Wood Materials Science & Engineering, in press, DOI: 10.1080/17480272.2020.1718205 (2019)

Predicting failure of notched cross-laminated timber plates including the effect of environmental stresses

John A. Nairn

Wood Science and Engineering, Oregon State University, Corvallis, OR 97330, USA

ARTICLE HISTORY
Compiled April 15, 2020

ABSTRACT
This paper derives analytical predictions for notched cross-laminated timber (CLT) plate delamination using fracture mechanics for crack propagation from the notch root. The analysis accounts for both CLT heterogeneity and residual stresses caused by seasonal variations in temperature and humidity. The accuracy of predictions coupled with shear corrections, was confirmed by comparison to finite element analysis. The fracture mechanics approach was validated as appropriate by comparison to recent experiments on notched CLT beams. Residual stress effects are significant and depend strongly on notch depth. Environmental changes that promote swelling, such as increases in temperature or moisture content, are more detrimental to plate integrity than are changes that promote shrinkage. Relatively modest levels of swelling stress can potentially cause spontaneous delamination. A new design guide for notched CLT plates that includes effects of heterogeneity and residual stresses is proposed.

Submitted: 09 Aug 2019, Accepted: 15 Jan 2020, Published online: 03 Feb 2020

KEYWORDS
CLT; Delamination; Fracture Mechanics; Residual Stresses

1. Introduction

Cross-laminated timber (CLT) is a relatively new composite mass-timber product comprised of cross-laminated layers of dimensioned lumber glued on the faces between layers. Despite some similarities in manufacturing processes, CLT is very distinct from glue-laminated timber beams (Glulam) or laminated veneer lumber (LVL). Compared to Glulam and LVL, where grain direction is the same in all layers, CLT has a heterogeneous structure consisting of alternating layers with 0° and 90° grain directions. The heterogeneity of CLT has two consequences. First, it causes new failure modes where type of failure depends on whether it occurs within a 0° or 90° layer. Second, whenever CLT experiences changes in moisture or temperature, differential moisture or thermal expansion properties between layers will cause internal residual stresses. Because many wood product failures are caused by changes in environmental conditions, all failure analyses for CLT must account for residual stresses that develop during lifetime of a structure.

This paper examines one problem — the design of notched CLT plates. The methods that have been successfully used for Glulam or LVL cannot automatically be extended to CLT problems. For example, failure depends on whether the notch is within a 0° layer of

CONTACT J. A. Nairn. Email: john.nairn@oregonstate.edu

a 90° layer and that issue does not occur in Glulam or LVL (Serrano 2018, Serrano *et al.* 2019). One analysis option for notched CLT plates is to use numerical methods, such as finite element analysis (FEA) (Serrano 2018, Serrano *et al.* 2019). Although FEA could work, it would not provide practical design equations. A better option for design guides is to derive analytical results using beam theory. Williams (1988), Schapery and Davidson (1990), and Hutchinson and Suo (1992) derived general methods for calculating energy release rates for crack propagation in layered specimens. Schapery and Davidson (1990) and Hutchinson and Suo (1992) considered heterogeneous beams. Williams (1988) considered only homogeneous beams, but it is trivial to extend it to include heterogeneity. This author extended these prior beam methods to include both heterogeneity and residual thermal stress (Nairn 1997, 2006).

The analysis here extends the beam methods of Nairn (2006) to include moisture-induced residual stresses common in wood products. These new methods were then used to derive analytical expressions for energy release rate for crack growth in CLT plates as a function of notch depth accounting for both heterogeneity and residual stresses. The accuracy of beam theory results was confirmed by comparison to FEA calculations. The FEA calculations revealed that beam theory calculations for mechanical loads need corrections for shear deformation. A prior shear correction developed by Gustafsson (1988) for homogeneous beams was found to be reasonably accurate for heterogeneous CLT plates. FEA calculations also showed that beam theory results for residual stress effects are accurate without any corrections.

Once energy release rate is known, Gustafsson (1988) proposes that delamination of a notched, homogeneous beam can be predicted by equating that energy release rate for a crack length equal to notch width to an effective beam toughness. This paper's beam theory analysis allows that approach to now include both heterogeneity and residual stresses. The fracture mechanics failure criterion was confirmed to be appropriate for CLT plates by comparison to recent experiments (Serrano *et al.* 2019, Friberg 2017). It was then used to propose a conservative design guide for calculating the maximum load to avoid delamination in any notched CLT plate. The design guide requires input of both effective CLT toughness and the anticipated level of residual stresses to be seen by a plate during its lifetime.

The derived analytical expressions were enabled by assuming identical 0° and 90° layers, by assuming all layers are subjected to uniform changes in temperature and moisture content, and by assuming delamination is determined by total energy release rate for crack growth. The final section considers refinements that can relax these assumptions. The options considered include modeling of mixed-mode fracture, assessing the role of gradients in temperature and moisture content, considering layers with different mechanical and toughness properties, and accounting for non-glued edges and end grain patterns in the 90° layers.

2. Notched CLT Energy Release Rate

Figure 1 shows an x-y cross section of a CLT plate having a notch of width b and depth h_2 with a crack of length a (see Table 1 for a list of nomenclature). Failure of a notched plate is modeled by a crack starting at the notch root and propagating into the plate. Figure 1 shows such a crack between two layers, but the analysis considers notches of any depths and the crack at any locations within a layer. Observed crack length in a failed plate would be from the notch root, but for analysis purposes, "crack length" is measured from the bearing load P location and therefore includes both notch width (b) and crack

Table 1. Nomenclature for various terms used throughout this paper in approximate alphabetical order. CTE and CME refer to coefficients of thermal and moisture expansion. ERR refers to energy release rate.

Term	Definition	Term	Definition
a	Crack length	α_L, α_t	CTE of 0° & 90° layers
$\alpha_\varepsilon^{(i)}$, $\beta_\varepsilon^{(i)}$	Arm CTE & CME	$\alpha_\kappa^{(i)}$, $\beta_\kappa^{(i)}$	Arm curvature CTE & CME
B	Plate depth (z direction)	b	Notch width
β_L, β_t	CME of 0° & 90° layers	Δc	Moisture change
$C_\kappa^{(i)}$, $C_\varepsilon^{(i)}$, $D^{(i)}$	Layer i beam properties	ε	Axial strain
$\Delta\varepsilon_{res}$	Differential residual strain	E_L, E_t	Modulus of 0° & 90° layers
G	Energy release rates	g	ERR components
G_c	Toughness	G_{Ic}, G_{IIc}	Mode I and II toughnesses
G_{rel}	Dimensionless ERR	G_{RS}	Rolling shear modulus
h_1, h_2	Arm thicknesses	$h_3 = h$	Plate thickness
I_0	0° layer moment of inertia	I	Plate moment of inertia
κ	Curvature	λ	Ratio t_{90}/t_0
M_i	Moment	N_i, l_i	Axial force at l_i
n, $n-1$	Number of 0° & 90° layers	P	Bearing load
P_c	Contact force	P_{fail}	Failure load
P_{rel}	Dimensionless failure load	R	Ratio E_t/E_L
Σ_{res}	Residual stress energy term	$\sigma_{res}^{(i)\,2}$	Weighted residual strain
t_0, t_{90}	Thickness of 0° & 90° layers	ΔT	Temperature change
ω	Fraction layer removed	ξ	Fraction plate remaining
χ	Shear correction term	$(\cdot)_{con}$	When arms in contact
$(\cdot)^{(m)}$	Mechanical stress term	$(\cdot)^{(r)}$	Residual stress term
$(\cdot)_{sep}$	When arms separated	$(\cdot)^{(x)}$	Cross term

propagation into the plate ($a-b$). The layers indicate a symmetric ($2n-1$) layer plate made by alternating n 0° layers of thickness t_0 with ($n-1$) 90° layers of thickness t_{90}. A small region of width δL around the crack tip is divided into three arms — arm 1 of thickness h_1 is above the crack, arm 2 of thickness h_2 is below the crack, and arm 3 is full plate to the right of the crack with thickness $h = h_3 = h_1 + h_2$. The plate's dimension in the z direction is B. Bearing load P is applied to the left edge as a consequence of structural forces. This modeling and prior experiments (Serrano *et al.* 2019, Friberg 2017) are for CLT beams with $B \sim h$, but the analysis applies to plates of any B subjected to the loading P along the z axis. For a general analysis, the load P along with other external loads are resolved into moments ($M_1^{(0)}$, $M_2^{(0)}$, and $M_3^{(0)}$) on the arms and point axial forces (N_1, N_2, and N_3 not shown in Fig. 1) at locations ℓ_1, ℓ_2, and ℓ_3. By force and moment equilibrium, the arm and full-beam resultants are:

$$M_1 = M_1^{(0)} + N_1\left(\frac{h_1}{2} - \ell_1\right) \quad M_2 = M_2^{(0)} + N_2\left(\frac{h_2}{2} - \ell_2\right)$$
$$N_3 = N_1 + N_2 \qquad M_3 = M_1^{(0)} + M_2^{(0)} - N_1(h_2 - \ell_3 + \ell_1) + N_2(\ell_3 - \ell_2)$$

Each arm is modeled in beam theory as having curvature, κ, and axial strain, ε_0, given by

$$\kappa = C_\kappa^{(i)} M + D^{(i)} N + \kappa_{res}^{(i)} \qquad \text{and} \qquad \varepsilon_0 = D^{(i)} M + C_\varepsilon^{(i)} N + \varepsilon_{res}^{(i)} \tag{1}$$

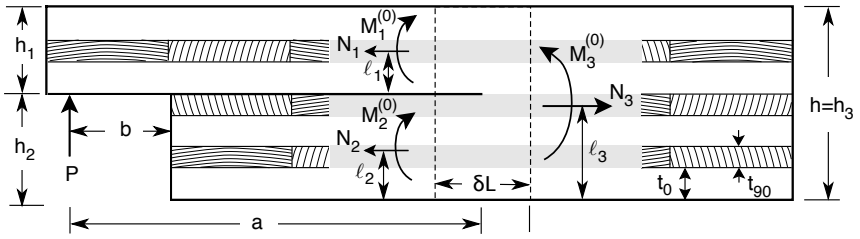

Figure 1. A section of CLT plate with a notch of width b and a crack of length a. The plate is divided into three multilayered arms with total thicknesses h_1, h_2, and $h = h_3$. Arms 1 and 2 are above and below the crack; arm 3 is the intact portion of the plate. In the crack-tip region, the arms have applied moments, $M_1^{(0)}$, $M_2^{(0)}$, and $M_3^{(0)}$, and normal forces. N_1, N_2, and N_3. The normal forces are applied at positions ℓ_1, ℓ_2, and ℓ_3, above the bottoms of the arms.

where $C_\kappa^{(i)}$ and $C_\varepsilon^{(i)}$ are curvature and mid-plane axial strain compliances, $D^{(i)}$ is a strain–curvature coupling compliance, and $\kappa_{res}^{(i)}$ and $\varepsilon_{res}^{(i)}$ are curvatures and axial strains caused by thermal and moisture expansion:

$$\kappa_{res}^{(i)} = \alpha_\kappa^{(i)}\Delta T + \beta_\kappa^{(i)}\Delta c \qquad \text{and} \qquad \varepsilon_{res}^{(i)} = \alpha_\varepsilon^{(i)}\Delta T + \beta_\varepsilon^{(i)}\Delta c$$

Here $\alpha_\kappa^{(i)}$ and $\alpha_\varepsilon^{(i)}$ are curvature and linear thermal expansion coefficients while $\beta_\kappa^{(i)}$ and $\beta_\varepsilon^{(i)}$ are curvature and linear moisture expansion coefficients. ΔT and Δc are constant temperature and moisture content differentials leading to residual stresses (a method for dealing with gradients in ΔT and Δc is discussed below). The moments in Fig. 1 are positive with positive κ defined as upward curvature. The coupling term, $D^{(i)}$, and the curvature expansion coefficients, $\alpha_\kappa^{(i)}$ and $\beta_\kappa^{(i)}$, are non-zero only for non-symmetric, heterogeneous arms.

The exact energy release rate for a notched CLT plate with residual stresses subjected only to traction loads, $\boldsymbol{T}^0$, is given by (Nairn 2006, 1997):

$$G = \frac{1}{B}\frac{d}{da}\left(\frac{1}{2}\int_S \boldsymbol{T}^0 \cdot u^m\, dS + \int_S \boldsymbol{T}^0 \cdot u^r\, dS + \frac{1}{2}\int_V \boldsymbol{\sigma}^r \cdot (\boldsymbol{\alpha}\Delta T + \boldsymbol{\beta}\Delta c)\, dV\right)$$

where u^m and u^r are displacements due to mechanical and residual stresses and $\boldsymbol{\sigma}^r$ are the residual stresses. Each integral can be evaluated over the dotted region of width δL in Fig. 1. Differentiation of that result gives energy release rate. The process is explained in Nairn (2006). The only changes here were to include moisture-induced residual stresses, which is trivially accomplished by replacing $\alpha_\kappa^{(i)}\Delta T$ and $\alpha_\varepsilon^{(i)}\Delta T$ in Nairn (2006) with $\kappa_{res}^{(i)}$ and $\varepsilon_{res}^{(i)}$, and to restrict attention to symmetric CLT plates (such that $D^{(3)} = \kappa_{res}^{(3)} = 0$). The general energy release rate for crack growth becomes

$$\begin{aligned} G = \frac{1}{2B}\Bigg[& \frac{(C_\kappa^{(1)}M_1 + \kappa_{res}^{(1)})^2}{C_\kappa^{(1)}} + \frac{(C_\kappa^{(2)}M_2 + \kappa_{res}^{(2)})^2}{C_\kappa^{(2)}} - C_\kappa^{(3)}M_3^2 + C_\varepsilon^{(1)}N_1^2 + C_\varepsilon^{(2)}N_2^2 \\ & - C_\varepsilon^{(3)}N_3^2 + 2D^{(1)}M_1N_1 + 2D^{(2)}M_2N_2 + 2\varepsilon_{res}^{(1)}N_1 + 2\varepsilon_{res}^{(2)}N_2 - 2\varepsilon_{res}^{(3)}N_3 \\ & - Bh_1E_c^{(1)}{\sigma_{res}^{(1)}}^2 - Bh_2E_c^{(2)}{\sigma_{res}^{(2)}}^2 + Bh_3E_c^{(3)}{\sigma_{res}^{(3)}}^2 \Bigg] \end{aligned}$$

Here $E_c^{(i)}$ is effective axial modulus of arm i and ${\sigma_{res}^{(i)}}^2$ is variance of the modulus-weighted residual strain in the arm (Nairn 2006). Note that this analysis is simple beam theory that

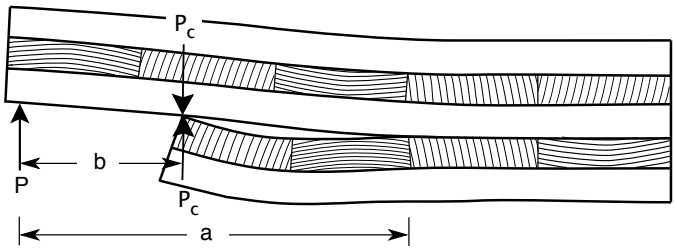

Figure 2. When residual stresses cause arms 1 and 2 to curve towards each other and load P is insufficient to separate them, a contact force P_c is induced at position b. This contact force leads to an opened crack plane up to crack tip at position a. The arm displacements were exaggerated for clarity.

ignores shear forces and deflections caused by those forces; a shear correction is given below.

3. Results and Discussion

3.1. *CLT Plate Results*

For loading by mechanical forces that result only in applied moments, the plate in Fig. 1 has $N_1 = N_2 = N_3 = 0$. In the presence of residual stresses, the total energy release rate becomes:

$$G^{(tot)} = \frac{1}{2B}\left(\frac{(C_\kappa^{(1)}M_1 + \kappa_{res}^{(1)})^2}{C_\kappa^{(1)}} + \frac{(C_\kappa^{(2)}M_2 + \kappa_{res}^{(2)})^2}{C_\kappa^{(2)}} - C_\kappa^{(3)}(M_1 + M_2)^2\right) + \Sigma_{res}$$

where

$$\Sigma_{res} = \frac{1}{2}\left(h_3 E_c^{(3)} {\sigma_{res}^{(3)}}^2 - h_1 E_c^{(1)} {\sigma_{res}^{(1)}}^2 - h_2 E_c^{(2)} {\sigma_{res}^{(2)}}^2\right)$$

The indicated moments are $M_1 = Pa$ and $M_2 = 0$, but a complication when dealing with residual stresses is that if the two arms curve towards each other (which happens whenever $\kappa_{res}^{(2)} - \kappa_{res}^{(1)} > 0$), and applied load is too low to separate them, the arms will be in contact at the notch root (distance b from the load). This situation is illustrated in Fig. 2 and was analyzed in Nairn (2006) by adding contact force P_c such that moment $M_c = P_c(a - b)$ is added to arms 1 and 2. In other words, contact changes the moments to $M_1 = Pa + M_c$ and $M_2 = -M_c$ where M_c to prevent interpenetration was derived to be:

$$M_c = \frac{3(\kappa_{res}^{(2)} - \kappa_{res}^{(1)}) - (2a + b)C_\kappa^{(1)}P}{2(C_\kappa^{(1)} + C_\kappa^{(2)})} \tag{2}$$

For positive P, contact occurs at any load with $M_c > 0$ or for

$$P < \frac{3(\kappa_{res}^{(2)} - \kappa_{res}^{(1)})}{(2a + b)C_\kappa^{(1)}} \tag{3}$$

For loads above this P, the arms are separated and $M_c = 0$.

For separated arms, total energy release rate reduces to

$$G_{sep}^{(tot)} = g_{sep}^{(m)} P^2 (a + \chi h)^2 + g_{sep}^{(x)} P (a + \chi h) + g_{sep}^{(r)} \tag{4}$$

where $g_{sep}^{(m)}$, $g_{sep}^{(x)}$, and $g_{sep}^{(r)}$ are energy release rate components due to mechanical loads, to an interaction between mechanical loads and residual stress, and to residual stresses, respectively. They are defined by:

$$g_{sep}^{(m)} = \frac{C_\kappa^{(1)} - C_\kappa^{(3)}}{2B}, \quad g_{sep}^{(x)} = \frac{\kappa_{res}^{(1)}}{B} \quad \text{and} \quad g_{sep}^{(r)} = \frac{1}{2B}\left(\frac{{\kappa_{res}^{(1)}}^2}{C_\kappa^{(1)}} + \frac{{\kappa_{res}^{(2)}}^2}{C_\kappa^{(2)}} \right) + \Sigma_{res}$$

Note that a was replaced by $(a + \chi h)$ to anticipate beam theory corrections described below. When the arms are in contact and $b = a$, total energy release rate decreases to:

$$G_{con}^{(tot)} = G_{sep}^{(tot)} - \frac{3\left(C_\kappa^{(1)} P (a + \chi h) - (\kappa_{res}^{(2)} - \kappa_{res}^{(1)})\right)^2}{8B(C_\kappa^{(1)} + C_\kappa^{(2)})} \tag{5}$$

Note that when $a \to b$ (which is used in design to predict initiation of failure from the notch root), the contact-force induced moment suggests that $M_c = P_c(a - b) = 0$. The contact analysis in Nairn (2006), however, shows that $P_c \to \infty$ as $a \to b$ while their product $M_c = P_c(a - b)$ is finite and nonzero (see Eq. (2) with $b = a$).

All terms above are easily found by composite beam analysis (see the appendix). The physical properties needed for each layer are thickness, t_j, modulus, E_j, thermal expansion coefficient, α_j, and moisture expansion coefficient, β_j, all along the plate's x axis. In terms of properties for layer j and k in arm i, the variance term needed for residual stress effects simplifies to:

$$h_i E_c^{(i)} {\sigma_{res}^{(i)}}^2 = \frac{\sum_{j,k;j<k} E_j E_k t_j t_k (\alpha_j \Delta T + \beta_j \Delta c - \alpha_k \Delta T - \beta_k \Delta c)^2}{\sum_j E_j t_j} \tag{6}$$

This equation is derived in Nairn (2006), but modified here to add moisture strains.

Although any combination of layers could be analyzed, one goal here was to derive analytical results. To achieve that goal, the analysis was restricted to CLT plates comprised of identical 0° layers alternating with identical 90° layers. The 0° layer properties are denoted as t_0, E_L, α_L, and β_L indicating properties in the longitudinal direction of wood. The 90° layer properties are denoted as t_{90}, E_t, α_t, and β_t, indicating properties in the transverse direction of wood. Whether these properties are tangential, T, radial, R, or someplace between tangential and radial properties depends on end-grain patterns of the timber in the 90° layers.

The remaining tasks were to find $C_\kappa^{(3)}$, $C_\kappa^{(1)}$, $C_\kappa^{(2)}$, $\kappa_{res}^{(1)}$, $\kappa_{res}^{(2)}$, and Σ_{res} for all possible notch depths. First, $C_\kappa^{(3)}$ is independent of notch depth and for a plate with n 0° layers can be simplified to:

$$C_\kappa^{(3)} = \frac{1/(E_L I_0)}{(1+\lambda)^2\left((1+R\lambda)n^3 - 3R\lambda n^2\right) + \lambda\left(3(1+\lambda)R\lambda - (2+\lambda)(1-R)\right)n - R\lambda^3} \tag{7}$$

where $I_0 = Bt_0^3/12$, $R = E_t/E_L$, and $\lambda = t_{90}/t_0$. For a plate with equal-thickness layers,

this result simplifies to

$$C_\kappa^{(3)}(\lambda=1)=\frac{1}{E_L I_0\Big[4(1+R)n^3-12Rn^2-3(1-3R)n-R\Big]}$$

For a solid wood beam (or for Glulam or LVL with all 0°layers), this result simplifies to the homogenous beam result of $C_\kappa^{(3)}(R=1)=12/(BE_Lh_3^3)$. The expression for $C_\kappa^{(3)}$ in Eq. (7), like all results quoted below, was derived by substituting alternating CLT layer properties into beam equations (see the appendix) and simplifying in Mathematica (Wolfram Research 2017). The process was tedious but straight forward. Only final forms, which were simplified as much as possible, are quoted here.

All remaining quantities can be found by evaluating two cases — a notch that ends within a 0° layer or a notch that ends within a 90° layer. For each case, let ω be the fraction of that layer removed by the notch where $0\le\omega\le1$. Each case needs to evaluate ${\sigma_{res}^{(i)}}^2$ for each arm for input to Σ_{res}. Imagine a square matrix with a row for each layer in an arm (counting the layer of fraction ω as one layer) and the summand of Eq. (6) in row j and column k of that matrix. For identical layers, this matrix is populated by either zeros (when layers j and k are in the same direction) or by a constant term (when layers j and k are in different directions). Evaluation of ${\sigma_{res}^{(i)}}^2$ is thus reduced to counting the number of non-zero elements in the upper half of the matrix and scaling fractional layer terms by ω to account for their reduced thickness The results can be enumerated to:

$$h_iE_c^{(i)}{\sigma_{res}^{(i)}}^2=E_Lt_0R\lambda(\Delta\varepsilon_{res})^2\begin{cases}\dfrac{n_i(n_i+\omega)}{n_i(1+R\lambda)+\omega} & [0/90/0.../0(\omega)]\\ \dfrac{n_i(n_i-1+\omega)}{n_i(1+R\lambda)-(1-\omega)R\lambda} & [0/90/0.../90(\omega)]\end{cases}\tag{8}$$

where $\Delta\varepsilon_{res}=\alpha_t\Delta T+\beta_t\Delta c-\alpha_L\Delta T-\beta_L\Delta c$ and n_i is number of 0° layers (not counting a fractional 0° layer). Note that $\Delta\varepsilon_{res}$ is the differential free-expansion strain between the 0° and 90° layers; it is not strain seen in the CLT panel. The second form with $n_i=n$ and $\omega=0$ (or first with $n_i=n-1$ and $\omega=1$) corresponds to the full plate term:

$$h_3E_c^{(3)}\sigma_{res}^{(3)2}=E_Lt_0R\lambda(\Delta\varepsilon_{res})^2\frac{n(n-1)}{n(1+R\lambda)-R\lambda}$$

The remaining notch-specific terms are listed next.

Notch top within a 0° layer: For this location, explicit expressions for $C_\kappa^{(2)}$ and the residual curvature term $\kappa_{res}^{(2)}$ for arm 2 reduce to:

$$C_\kappa^{(2)}=\frac{1}{E_LI_0W^{(2)}}\quad\text{and}\quad\kappa_{res}^{(2)}=-6R\lambda n_2\frac{(1-\omega)\big(n_2(1+\lambda)+\omega\big)}{n_2(1+R\lambda)+\omega}\frac{\Delta\varepsilon_{res}}{t_0W^{(2)}}\tag{9}$$

where

$$W^{(2)}=(1+\lambda)^2\big((1+R\lambda)n_2+3\omega\big)n_2^2+\big(3\omega^2+\big(3R\omega^2-2(1-3\omega)(1-R)\big)\lambda+2(1-R)\lambda^2\big)n_2+\omega^3-\frac{3(1-R)^2n_2^2\lambda^2(1-\omega)^2}{n_2(1+R\lambda)+\omega}$$

and n_2 is the number of complete 0° layers in arm 2. Note that a notch top within the first

$0°$ layer has $n_2 = 0$ and this result correctly simplifies to $C_\kappa^{(2)}(n_2 = 0) = 1/(E_L \omega^3 I_0)$. $C_\kappa^{(1)}$ and $\kappa_{res}^{(1)}$ are found by replacing ω with $1-\omega$, setting $n_2 = n_1$ (which is the number of complete $0°$ layers in arm 1 and $n_1 + n_2 = n-1$ for this case), and changing the sign for $\kappa_{res}^{(1)}$. Finally, Σ_{res} combines to:

$$\Sigma_{res} = \frac{\big((n-1)\omega - n_2\big)^2 E_L t_0 R^2 \lambda^2 (\Delta\varepsilon_{res})^2}{\big((n-n_2)(1+R\lambda) - R\lambda - \omega\big)\big(n_2(1+R\lambda)+\omega\big)\big(n(1+R\lambda) - R\lambda\big)} \tag{10}$$

Notch top within a 90° layer: For this location, explicit expressions for $C_\kappa^{(1)}$ and the residual curvature term $\kappa_{res}^{(1)}$ for arm 1 reduce to:

$$C_\kappa^{(1)} = \frac{1}{E_L I_0 W^{(1)}} \quad \text{and} \quad \kappa_{res}^{(1)} = 6R\lambda n_1 \frac{(1-\omega)\big(n_1(1+\lambda) - \lambda\omega\big)}{n_1(1+R\lambda) - \omega R\lambda} \frac{\Delta\varepsilon_{res}}{t_0 W^{(1)}} \tag{11}$$

where

$$W^{(1)} = (1+\lambda)^2\big((1+R\lambda)n_1 - 3R\lambda\omega\big)n_1^2 + \lambda\big(3\omega^2 R\lambda^2 + \big(3\omega^2 + 2(1-R)(1-3\omega)\big)\lambda - 2(1-R)\big)n_1 - R\lambda^3\omega^3 - \frac{3(1-R)^2 n_1^2 \lambda^2 (1-\omega)^2}{n_1(1+R\lambda) - \omega R\lambda}$$

$C_\kappa^{(2)}$ and $\kappa_{res}^{(2)}$ are found by replacing ω with $1-\omega$, setting $n_1 = n_2$ (note that $n_1 + n_2 = n$ for this case), and changing the sign for $\kappa_{res}^{(2)}$. Finally, Σ_{res} combines to

$$\Sigma_{res} = \frac{\big(n(1-\omega) - n_2\big)^2 E_L t_0 R^2 \lambda^2 (\Delta\varepsilon_{res})^2}{\big((n-n_2)(1+R\lambda) - \omega R\lambda\big)\big(n_2(1+R\lambda) - (1-\omega)R\lambda\big)\big(n(1+R\lambda) - R\lambda\big)} \tag{12}$$

3.2. *Mechanical Loading Alone*

In the absence of residual stresses, any positive P results in separated arms and energy release rate is always given by $G^{(m)} = g_{sep}^{(m)} P^2 (a + \chi h)^2$. A fracture mechanics prediction of failure follows by equating $G^{(m)}$ to an effective CLT toughness G_c and solving for P. Guided by the forms of $C_\kappa^{(1)}$ and $C_\kappa^{(3)}$ for all crack locations, the failure prediction for mechanical stress alone can be written as:

$$P_{fail}^{(m)} = \frac{P_{rel}^{(m)} \sqrt{2BE_L I_0 G_c}}{a} \quad \text{where} \quad \frac{1}{P_{rel}^{(m)}} = \left(1 + \frac{\chi h}{a}\right) \sqrt{E_L I_0 \left(C_\kappa^{(1)} - C_\kappa^{(3)}\right)} \tag{13}$$

is a dimensionless, relative failure load. From $P_{rel}^{(m)}$ for a $(2n-1)$-layer CLT plate with a given number of broken layers (n_2), notch depth location (ω), λ, R, and beam-theory correction ($\chi h/a$), failure load can be predicted for any values of a, B, E_L, I_0, and G_c. The prediction is applied to a notched plate by setting initial crack length a equal to the notch width b.

Equation (13) combined with Eqs. (7) and (11) provides analytical expressions for notched plate failure for any notch depth. Figure 3A plots $P_{rel}^{(m)}$ as a function in notch depth for plates from 3 to 9 layers using $\lambda = 1$, $R = 500/12000 = 0.0417$, and $\chi = 0$. The notch depth is plotted as number of removed layers ranging from half the first $0°$

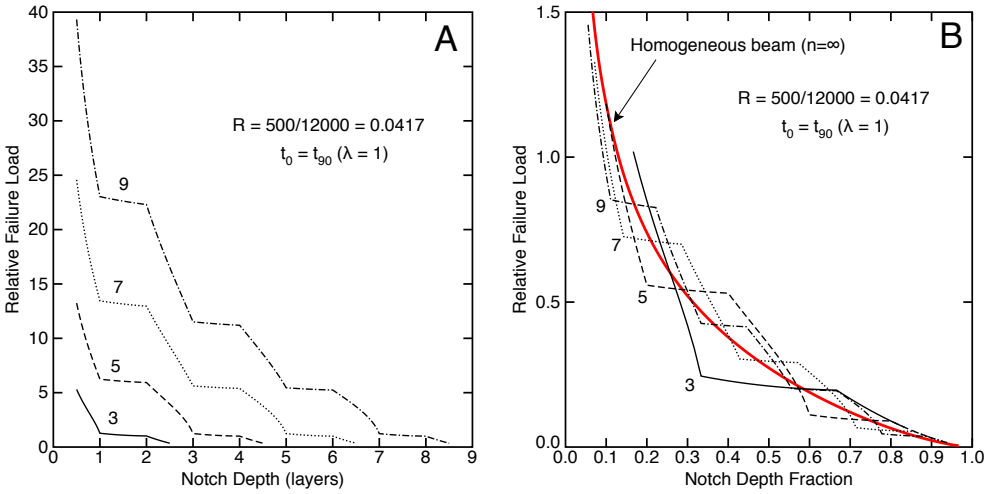

Figure 3. A. Dimensionless failure load, P_{rel}, for mechanical loads only as a function of number of layers removed in CLT plates with 3, 5, 7, and 9 equal-thickness layers. B. An alternate dimensionless failure load, $P_{rel,2}$, for mechanical loads only as a function of plate fraction removed for CLT plates with constant total thickness but variable thickness layers. The thick line is for a CLT plate with an infinite number layers or for a homogeneous plate with axial modulus of all layers equal to rule-of-mixture modulus E_c.

layer up to all removed except half the last 0° layer. The failure load has a stair-step shape with corners when the notch top is at a 0°/90° interface. This shape is a consequence of plate heterogeneity. The failure load drops rapidly when notch ends within a 0° layer and then plateaus at nearly constant load when notch ends within a 90° layer. For notches within a 0° layer, cracks are expected to proceed along the plate's x axis as directed by wood grain direction in 0° layers. For notches within 90° layers, however, cracks are free to run in any direction through the transverse cross-section of wood. Because $P_{rel}^{(m)}$ for a crack growing at the top of a 90° layer is slightly lower than for a crack at the bottom (*i.e.*, $G^{(m)}$ increases as a crack moves from bottom to top of a 90° layer), the prediction is that a notch cut anywhere within a 90° layer will fail by a crack that diverts to the top of that layer and then follows the grain direction at the bottom of the next 0° layer. This prediction agrees with experimental observations (Serrano *et al.* 2019, Friberg 2017).

Figure 3A shows that $P_{rel}^{(m)}$ increases as the number of layers increases. This effect is simply because for a given notch depth, a CLT plate with more layers has more material remaining to carry load. An alternate comparison is to plot failure load for CLT plates of constant total thickness $h = h_3$ as a function of the number of layers; plates with more layers have thinner layers of thickness $t_0 = h/(n(1+\lambda)-\lambda)$. To compare plates with different t_0, a better dimensionless form is:

$$P_{fail}^{(m)} = \frac{P_{rel,2}^{(m)}\sqrt{2BE_L I G_c}}{a} \quad \text{where} \quad \frac{1}{P_{rel,2}^{(m)}} = \left(1+\frac{\chi h}{a}\right)\sqrt{E_L I\left(C_\kappa^{(1)} - C_\kappa^{(3)}\right)} \tag{14}$$

where $I = Bh^3/12$ replaces I_0. Figure 3B plots $P_{rel,2}^{(m)}$ as a function of plate fraction removed by the notch. The stair-step shape remains, but step widths decrease as the number of layers increases. The smooth line plots $P_{rel,2}^{(m)}$ as $n \to \infty$, which is equivalent to a homogeneous plate with axial modulus given by average of 0° and 90° layer moduli or $E_c = E_c^{(3)}(n \to \infty) = E_L(1+R\lambda)/(1+\lambda)$. Using Eq. (14) with $C_\kappa^{(3)} = 1/(E_c I)$ and $C_\kappa^{(1)} = 1/(E_c I \xi^3)$, where $\xi = h_1/h$ is plate fraction remaining above the notch, the dimen-

sionless failure load for a homogeneous plate is:

$$\frac{1}{P^{(m)}_{rel,2,n\to\infty}} = \left(1+\frac{\chi h}{a}\right)\sqrt{\frac{1+\lambda}{1+R\lambda}\left(\frac{1}{\xi^3}-1\right)} \tag{15}$$

Deviations between $P^{(m)}_{rel,2}$ in CLT plates *vs*. homogeneous plates quantifies errors caused by design methods that ignore heterogeneity. A design based on homogeneous plates would over predict strength whenever the notch is at or near the bottom of a 90° layer and under predict it when the notch is at or near the bottom of 0° layer. The magnitude of the errors, especially when using many layers, might suggest that designs based on homogeneous plates with suitable safety factors would be acceptable. But that approach is unacceptable whenever a plate experiences residual stresses caused by changes in temperature or moisture content. Residual stress effects are considered below.

3.3. *Verification of Beam Theory Calculations*

To verify that analytical beam theory is accurate for finding energy release rate, the predictions were compared to finite element analysis (FEA) of a 5-layer CLT plate. The layer thicknesses were $t_0 = t_{90} = 40$ mm ($\lambda = 1$) for total plate thickness of 200 mm. The FEA modeled a symmetric three point bending specimen of length 3200 mm or aspect ratio of 16 with notch width $b = 320$ mm and crack length $a = 640$ mm. The orthotropic wood properties (Serrano 2018) used in FEA calculations are listed in Table 2. Half the specimen (by symmetry) was meshed using 10 × 10 mm, 8-node, quadratic elements in 2D, plane stress analyses resulting in 4 elements across each layer. The energy release rate was found using crack closure (Nairn 2011). Because exact solutions for pure bending result in quadratic variations in arm displacements, quadratic elements converge extremely well in bending problems while linear elements converge much slower (Nairn 2011). The 10 × 10 mm elements were confirmed to be converged results by observing that doubling resolution did not change energy release rate results. Although it is common to refine meshes around crack tips in the hopes of improved accuracy, that approach is counterproductive in bending problems. Mesh refinement always uses elements that distort spatial coordinates through isoparametric transformations. Those distortions cause those elements to represent quadratic variations in displacement less accurately than would a mesh of larger, equally-sized rectangular elements. All calculations were done with the public domain NairnFEA software (Nairn 2019).

Figure 4 compares beam theory results (solid lines) to FEA calculations (symbols) using two different boundary conditions. The FEA calculations were done for cracks at each 0°/90° interface and at each layer's mid-plane. First, the plate was loaded with a point load as illustrated in Fig. 1. The FEA results (square symbols) predicted lower load than uncorrected beam theory ($\chi = 0$) with maximum difference of 29.8%. This difference is caused by beam theory ignoring effects of shear deformation when $\chi = 0$. Furthermore, in materials with high E/G ratio ($E_L/G_L = 20$ in 0° layers and $E_t/G_{RS} = 8.33$ in 90° layers), shear effects can be significant. To verify that differences were caused by shear effects, FEA calculations were repeated by end loading the plate with a pure moment, which was done by applying an axial stress that varied from $+\sigma = 6Pa/(Bh_1^2)$ to $-\sigma$ on the left edge or arm 1 such that moment resultant was $M = Pa$. All beam theory ($\chi = 0$) results were within 0.3% of the "Moment Load" FEA results (circles).

In brief, the beam analysis methods are accurate, but they do no account for shear deflections. Two options to account for shear are 1) extend heterogenous beam analy-

Table 2. FEA Properties for 0° and 90°layers[a]. The 90° layers assumed tangential wood direction in the x direction. All layers assumed radial wood direction in the y direction.

Property	Value	Property	Value
$E_{xx}^{(0)} = E_L$	12000 MPa	$E_{xx}^{(90)} = E_t$	500 MPa
$E_{yy}^{(0)}$	600 MPa	$E_{yy}^{(90)}$	600 MPa
$G_{xy}^{(0)} = G_L$	600 MPa	$G_{xy}^{(90)} = G_{RS}$	60 MPa
$\nu_{xy}^{(0)}$	0.427	$\nu_{xy}^{(90)}$	0.35
$\beta_x^{(0)} = \beta_L$	0.0	$\beta_x^{(90)} = \beta_t$	0.26 c^{-1}
$\beta_y^{(0)}$	0.13 c^{-1}	$\beta_y^{(90)}$	0.13 c^{-1}

[a]Thermal expansion coefficients were not used in FEA calculations.

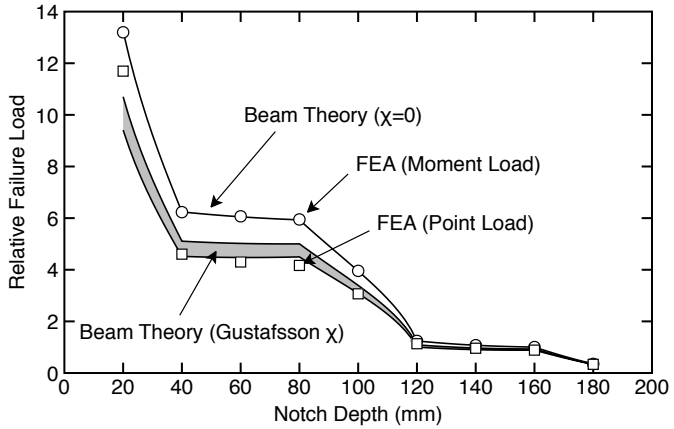

Figure 4. The solid lines are beam theory calculations for P_{rel} due to mechanical loads only. The $\chi = 0$ line is uncorrected beam theory; the "using χ" curves are corrected using the Gustafsson (1988) method. The shaded region corresponds to correction for shear modulus between the lower bound (bottom line) and upper bound (top line) values. The symbols are FEA calculations for energy release rate. The circles are when applying a moment to the end of arm 1; the squares for for a point load applied at the bottom or arm 1.

sis to account for shear; 2) use prior methods to correct beam theory for homogeneous, anisotropic beams. The second option was used here and two prior results are available. Both, Hashemi *et al.* (1990) and Gustafsson (1988), claimed that simple beam theory for homogeneous beams can be corrected for shear deflections (and some other deflections) by defining an *effective* crack length $a_{eff} = a + \chi h$, where χ is defined by

$$\chi = \begin{cases} \sqrt{\frac{E_x}{11G_{xy}}\left(3-2\left(\frac{\Gamma}{1+\Gamma}\right)^2\right)} \quad \text{and} \quad \Gamma = \frac{1.18\sqrt{E_x E_y}}{G_{xy}} & \text{Hashimi } et\ al. \\ \sqrt{\frac{E_x \xi^2}{10G_{xy}(1+\xi+\xi^2)}} & \text{Gustafsson} \end{cases}$$

Here E_x, E_y, and G_{xy} are homogenized properties of the full CLT plate. While $E_x = E_c^{(3)}$ and $E_y = E_t$ should be accurate for the modeled CLT plates, calculation of G_{xy} is more difficult. Rather than attempt analytical or numerical modeling for G_{xy}, one can use composite bounding methods where trivial bounds on G_{xy} (found by subjecting layers to either constant shear stress or constant shear strain (Hashin 1969)) are:

$$\frac{n+(n-1)\lambda}{\frac{n}{G_L}+\frac{(n-1)\lambda}{G_{RS}}} \leq G_{xy} \leq \frac{nG_L+(n-1)\lambda G_{RS}}{n+(n-1)\lambda}$$

Here G_L is wood longitudinal shear modulus in the 0° layers and G_{RS} is wood rolling shear modulus in the 90° layers.

The shaded area in Fig. 4 shows the range in corrected beam theory results calculated using the Gustafsson (1988) χ with either upper bound G_{xy} (top curve) or lower bound G_{xy} (lower curve). This homogeneous correction applied to beam theory provides a satisfactory result for failure load in heterogeneous CLT plates. The specific model used for G_{xy} has relatively small effect, but the lower bound G_{xy} correction is closer to FEA than the upper bound G_{xy}.

The Hashemi *et al.* (1990) correction did not work as well. The Gustafsson (1988) method is preferred because the correction depends on notch depth through ξ while the Hashemi *et al.* (1990) correction is independent of notch depth. A comparison of simple beam theory to FEA results verifies that the correction should depend on notch depth. That comparison also shows that a homogeneous correction is an approximation that misses some heterogeneity effects. In brief, the homogeneous χ is too high for cracks at the top of 0° layers and too low for cracks at the top of 90° layers. This effect shows up more for short a (or larger h/a), but overall the correction works reasonably well for any crack length. While a homogeneous correction is used here and judged satisfactory, the beam theory analysis could potentially be improved by deriving heterogeneous correction terms.

Finally, note that substituting the Gustafsson (1988) χ into Eq. (15) with $R = 1$ (*i.e.*, for Glulam), the homogeneous beam result can be written as:

$$\frac{P_{fail,2,n\to\infty}^{(m)}}{Bh_1} = \frac{\sqrt{\frac{G_c}{h}}}{\sqrt{\frac{0.6}{G_{xy}}\xi(1-\xi)}+\frac{a}{h}\sqrt{\frac{6}{E_c}\left(\frac{1}{\xi}-\xi^2\right)}}$$

which is identical to Gustafsson (1988) and the basis for Eurocode 5 (1995). In other words, this analysis is identical to prior methods for homogeneous beams but now extends those methods to account for heterogeneity and subsequent sections extend it to account for residual stresses.

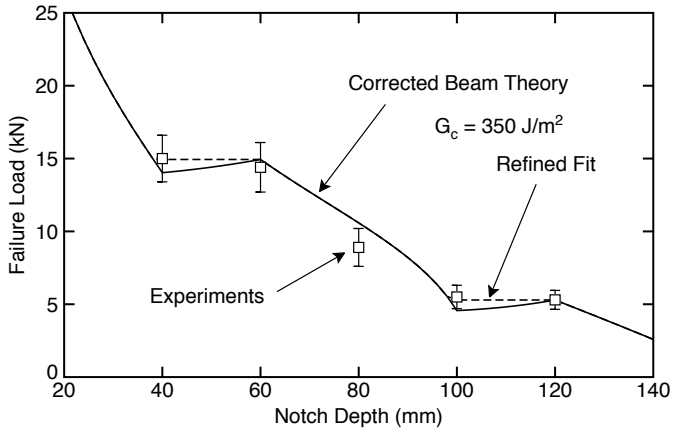

Figure 5. Fit of failure predictions to experimental results in Serrano *et al.* (2019) and Friberg (2017). The best fits used $G_c = 350$ J/m^2. The solid line is fit using Eq. (13); the dashed line is a refined fit that assumes a notch in the 90° layer fails as if the entire 90° layer was removed.

3.4. *Validation of Fracture Mechanics Methods*

The previous section verified that corrected beam theory accurately calculates energy release rate, but a question remains — can notched plate delamination be predicted by energy release rate for crack growth at the notch corner? Answering this question requires model validation by comparison to experiments. Here the predictions were compared to recent experiments in Serrano *et al.* (2019) and Friberg (2017). The experiments were on five-layer CLT beams with $t_0 = 40$ mm and $\lambda = 0.5$. The layer properties from Serrano (2018) are in Table 2. By varying G_c, experimental results were fit to predictions by Eq. (13) using χ determined with a lower bound G_{xy}. The fitting process assumed that plates were tested soon after fabrication such that $\Delta T = \Delta c = 0$ or that the mechanical-loading-only analysis is acceptable. The best-fit results in Fig. 5 show that a fracture mechanics failure model fits experiments well.

The best-fit toughness of $G_c = 350$ J/m^2 falls within the range of mode I (Schniewind and Pozniak 1971, Wilson *et al.* 2013) and mode II (Conrad *et al.* 2003, Stanzl-Tschegg *et al.* 1996, Yoshihara 2004) toughness values for typical wood species and is therefore a reasonable value for the mixed-mode crack growth expected by point load within a notch. This analysis assumed failure occurs at a critical, *total* energy release rate and therefore ignored any effects of varying mode mixity caused by changes in notch depth. Possible consequences of ignoring mode mixity are discussed below.

The predictions show a slight increase for failure load between a crack at the bottom or top of a 90° layer that is not seen in experiments. The experiments did show, however, that cracks at the bottom of a 90° layer failed by propagating quickly to the top of that layer (Serrano *et al.* 2019, Friberg 2017). From this observation, beam theory predictions could be refined by assuming that failure load for a crack at any location within a 90° layer equals the failure load for a notch that removes that entire layer. The dotted line in Fig. 5 illustrates this approach and improved the fit to experimental results. The uptick in predictions might also be a consequence of using a shear correction for a homogeneous beam; deriving a heterogeneous correction might improve predictions.

3.5. *Residual Stresses Alone*

Whenever one (or both) of the arms created by splitting a layered plate along a crack is a non-symmetric plate, residual stresses can cause that arm (or both arms) to curve as the crack propagates. This curvature contributes to energy release rate (Nairn 2006) that would predict spontaneous delamination without any applied load if it reaches toughness of the CLT plate. Because CLT is typically made with an odd number of alternating layers, every possible split location results in at least one non-symmetric arm. In contrast, because Glulam is made from identical layers, every split location results in two symmetric arms (*i.e.*, two thinner Glulam beams). Although design of notched Glulam beams can ignore internal stresses, design of notched CLT plates must always account for them. Note that Glulam beams may develop residual stresses due to differential shrinkage between radial and tangential directions within and between timber layers, but those internal stresses do not cause arm curvature and therefore have little or no effect on notch delamination.

Guided by the forms of $\kappa_{res}^{(i)\,2}/C_\kappa^{(i)}$ and Σ_{res} for each crack location, the energy release rate due to residual stresses alone is written as:

$$G^{(r)} = E_L t_0 (\Delta\varepsilon_{res})^2 G_{rel}^{(r)}$$

where

$$G_{rel}^{(r)} = \begin{cases} \dfrac{g_{sep}^{(r)}}{E_L t_0 (\Delta\varepsilon_{res})^2} & \text{if } \kappa_{res}^{(2)} - \kappa_{res}^{(1)} \le 0 \\ \dfrac{1}{E_L t_0 (\Delta\varepsilon_{res})^2}\left(g_{sep}^{(r)} - \dfrac{3(\kappa_{res}^{(2)} - \kappa_{res}^{(1)})^2}{8B(C_\kappa^{(1)} + C_\kappa^{(2)})} \right) & \text{if } \kappa_{res}^{(2)} - \kappa_{res}^{(1)} > 0 \end{cases}$$

is a dimensionless energy release rate. The two arms will separate under swelling conditions ($\Delta\varepsilon_{res} > 0$) or be in contact under shrinking conditions ($\Delta\varepsilon_{res} < 0$). Note that $G_{rel}^{(r)} \ge 0$ for both separated and contact arms, but it is always larger when arms separate. Thus heating or an increase in moisture content are more likely to promote delamination than is cooling or a decrease in moisture content.

Equating $G^{(r)}$ to effective CLT toughness, the differential strain to cause spontaneous delamination of a notched CLT plate is

$$|\Delta\varepsilon_{res}| = \sqrt{\frac{G_c}{E_L t_0 G_{rel}^{(r)}}} \tag{16}$$

Figure 6 plots $|\Delta\varepsilon_{res}|$ as a function of notch depth for plates with three or seven 40 mm layers for properties in Table 2 and $G_c = 350\,\text{J/m}^2$. The solid lines are analytical results for separated arms. The dashed lines are analytical results for arms in contact. The notches most prone to spontaneous delamination are the minima values that occur at layer interfaces. The notches least prone to delamination are the maxima near the mid-planes of layers. A crack at a layer mid-plane divides that layer between the two arms thereby reducing $\kappa_{res}^{(2)} - \kappa_{res}^{(1)}$ and $G_{rel}^{(r)}$. Note that notches at the mid-plane of 0° layers have more delamination resistance than notches at the mid-plane of 90° layers. The notch locations most prone for internal-stress-induced failure are depths two layers from either surface (at 40 or 80 mm for three-layer CLT and at 80 or 200 mm in seven-layer CLT). Those locations result in one arm being a bilayer strip that maximizes $\kappa_{res}^{(i)}$ among all possible sub-plates derived from the full CLT plate.

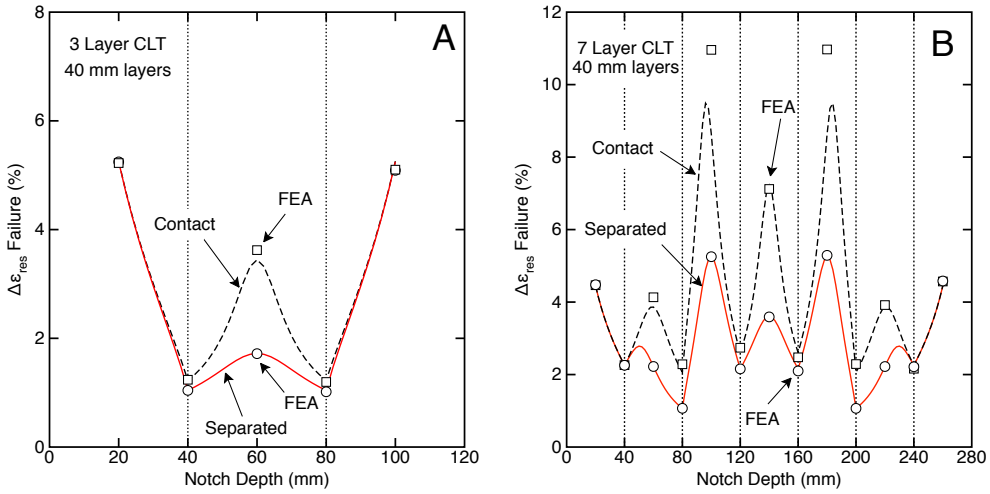

Figure 6. The residual strain, $|\Delta\varepsilon_{res}|$, to cause spontaneous failure as a function of notch depth for CLT plates with $G_c = 350$ J/m^2: A. Three-layer plate. B. Seven-layer plate. The solid lines are for $\Delta\varepsilon_{res} > 0$ such that the arms separate. The dashed lines are for $\Delta\varepsilon_{res} < 0$ such that the arms are in contact. The symbols are FEA calculations for separated arms (circles) or arms in contact (squares).

Energy release rates due to residual stresses were verified by FEA calculations using the above-mentioned methods but loading was replaced by uniform residual strain applied to each layer. The FEA results for interfaces and layer mid-planes are the open symbols in Fig. 6 (circles for separated arms and squares for arms in contact). The FEA results agreed well with beam theory without any corrections. The reason no shear corrections were needed was because $G_{rel}^{(r)}$ is independent of crack length. The FEA analysis for arms in contact required special handling. To avoid the need for contact elements (which is a non-linear effect not available in the linear elastic FEA software that was used), FEA calculations with $\Delta\varepsilon_{res} < 0$ set the nodes at the contact point to zero displacement in the y direction while the nodes on the plate's right edge had zero deflection only in the x direction to define the plate's symmetry direction. This approach worked well for all locations except for the mid-plane of the central layer of the three-layer CLT and the mid-planes of the three central layers in the seven-layer CLT. For these locations, parts of the arms near the contact point had interpenetration despite matching displacements at the contact point. These four locations were reevaluated by replacing the zero-displacement condition with contact force P_c as illustrated in Fig. 2. P_c was increased until the arms separated and then decreased by trial an error to the point of contact. With this modification, analytical and FEA results agreed well for the central 90° layer. An observable difference between analytical and FEA results remained for cracks in the middle of layers three and five of the seven-layer CLT, which are 0° layers. These differences were likely caused by treatment of arm contact.

Figure 6 shows that internal stresses should play a significant role in designing notched CLT plates. Plates exposed to residual strains as low as 1% may fail without any applied load. Typical wood species shrink in volume about 12% from green to dry, which is comprised of about 4% in the radial direction, 8% in the tangential direction, and 0% in the longitudinal direction (Forest Products Laboratory 2010). Thus a fraction of shrinkage seen in wood is enough to cause spontaneous failure. This calculation assumed $G_c = 350$ J/m^2. If a plate has a lower grade of timber near the notch root, if the notch root is near an adhesive bond with lower toughness than the wood, or if the plate has applied load, the residual strain to cause failure could be much lower. Notched CLT plate design

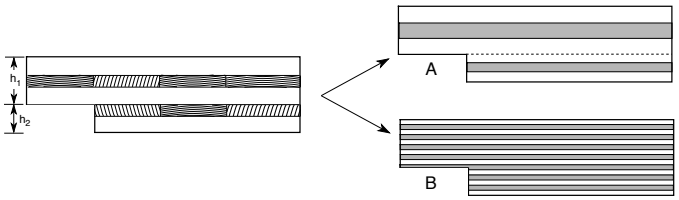

Figure 7. Residual stresses effects on notch delamination in the CLT plate on the left can be reduced by changing the lamination structure. A. Arm curvature effects are eliminated if the two arms on either side of the dashed failure plane are symmetric subplates. B. Thinner layers reduce residual stresses effects for any notch depth.

should always anticipate the maximum value of $\Delta\varepsilon_{res}$ that will be experienced over the plate's lifetime.

Two options to reduce residual stress effects on notch failure are illustrated in Fig. 7. First, the CLT plate can be customized such that the two arms on either side of the crack plane are symmetric CLT plates (the center layer could be two adjacent 0° layers or one extra-thick layer). Because symmetric arms have $\kappa_{res}^{(i)} = 0$, the energy release rate due to internal stresses is reduced to only the Σ_{res} term. Second, the CLT plate could be made using thinner layers. Thinner layers reduce $\kappa_{res}^{(i)}$ and Σ_{res}, which reduces energy release rate due to residual stresses. As seen by Eq. (16), the residual strain required for spontaneous delamination is inversely related to square root of layer thickness. The use of thinner layers is the preferred option. This option works for any depth notch while symmetric arms work for only one specific depth. Furthermore, thinner layers can reduce other effects of internal stresses such as layer cracking and delaminations at the tips of those cracks or at non-glued timber edges (Nairn 2018). Symmetric arms only reduce residual stress effects on notch failure.

3.6. *The Simplest Design Guide - Combined Mechanical and Residual Stress Loading*

Imagine that an installed, notched, CLT plate is anticipated to experience $\pm\Delta\varepsilon_{res}$ over its' lifetime. A conservative design guide for maximum load, P_{limit}, should assume failure when G_c equals the maximum energy release rate over that range of $\Delta\varepsilon_{res}$ values. That maximum is for swelling (use $|\Delta\varepsilon_{res}|$) and separated arms (use $G_{sep}^{(tot)}$ in Eq. (4)). The design limit load is then found by solving for P:

$$P_{limit} = \begin{cases} \frac{1}{a+\chi h}\left(\sqrt{\left(\frac{g_{sep}^{(x)}}{2g_{sep}^{(m)}}\right)^2 + \frac{G_c - g_{sep}^{(r)}}{g_{sep}^{(m)}}} - \frac{|g_{sep}^{(x)}|}{2g_{sep}^{(m)}}\right) & g_{sep}^{(r)} < G_c \\ 0 & g_{sep}^{(r)} \geq G_c \end{cases} \tag{17}$$

The zero value corresponds to a plate that would fail due to residual stresses alone (where the first equation would give a negative or imaginary result). Ignoring residual stresses, the limit load would match Eq. (13). Designing a structure to withstand both applied load and environmental stresses, however, should include $g_{sep}^{(x)}$ and $g_{sep}^{(r)}$ evaluated at the maximum anticipated value for $|\Delta\varepsilon_{res}|$.

Example P_{limit} calculations for a 200 mm thick CLT plate with timber properties in Table 2, notch width $a = b = 50$ mm, thickness $B = 100$ mm, and $G_c = 350$ J/m^2 are given in Fig. 8. The solid lines plot P_{limit} for $\Delta\varepsilon_{res}$ from 0% (ignoring residual stresses) to 3% for a conventional CLT plate having five 40 mm layers. Accounting for residual stresses, causes design limit loads for notches less that half way through the plate to drop from 10% to 66%, 27% to 100% (*i.e.*, spontaneous failure), and 46% to 100% for $\Delta\varepsilon_{res}$ from 1% to

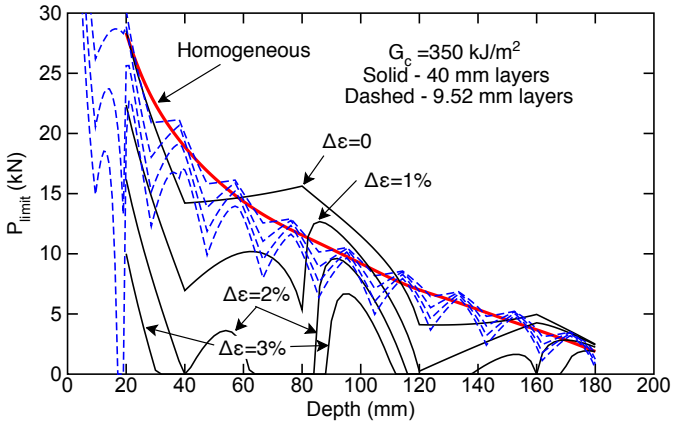

Figure 8. Limit load calculations using Eq. (17) for CLT plates for $\Delta\varepsilon_{res} = 0\%$, 1%, 2%, and 3% and with $G_c = 0.35$ J/m^2. The solid lines are for five-layer CLT with 40 mm layers. The dashed lines are for 21-layer CLT with 9.52 mm layers (top to bottom is for increasing $\Delta\varepsilon_{res}$). The thick line is for a homogeneous plate.

3%, respectively. The minimal drops are for notches about half way through the plate; the maximal drops are for notches that remove the first two layers or all but that last two layers. Considering overall transverse shrinkage of wood from 4% to 8% from green to dry (Forest Products Laboratory 2010), a long-lived structure might see $\Delta\varepsilon_{res} = 1\%$, could see $\Delta\varepsilon_{res} = 2\%$, but probably will not see $\Delta\varepsilon_{res} = 3\%$. Some value for $\Delta\varepsilon_{res}$ in this range should be used in design calculations.

A recommendation above to reduce residual stress effects on notch failure was to use thinner layers. The dashed lines repeat the calculations for a 21-layer CLT plate with 9.52 mm thick layers. This change signficantly reduces residual stress effects for notches in the range of 20 to 180 mm. The *maximum* decrease in failure load for notch depths from 20 to 100 mm due to residual stresses is reduced from 66%, 100%, and 100% with 40 mm layers to 13%, 26%, and 40% with 9.52 mm layers for $\Delta\varepsilon_{res}$ from 1% to 3%, respectively. Note that shallow notches less then 20 mm deep through thin layers are prone to residual-stress-induced failures for $\Delta\varepsilon_{res} = 3\%$. Finally, the thick, smooth curve is for a homogeneous plate and such a plate is not influenced by $\Delta\varepsilon_{res}$. Deviations from this curve characterize the consequences of ignoring heterogeneity and residual stresses in design calculations

All limit load calculations are conditions for initiation of delamination at the notch root. Because energy release rate due to mechanical loads and residual stresses increases or remains constant as the crack grows, once a crack starts it could rapidly delaminate all layers below the notch root. If the remaining CLT plate in arm 1 is sufficient to carry all loads, the delaminated layers may fall off, but the remaining plate would survive.

3.7. *Refinements*

The above calculations followed the Gustafsson (1988) approach that assumes failure when *total* energy release rate for crack propagation equals an effective CLT toughness, G_c. But the end loading in Fig. 1 induces mixed-mode loading where total $G = G_I + G_{II}$ and G_I and G_{II} are energy release rates due to tensile loading (mode I) and shear loading (mode II), respectively. A refinement that could improve the predictions would be to use a mixed-mode failure criterion $f(G_I, G_{II}, G_{Ic}, G_{IIc}) = 1$ where G_{Ic} and G_{IIc} are toughnesses for pure mode I or mode II loading. With such a criterion, failure occurs when f reaches 1, but implementing this refinement raises two issues.

First, analyzing mixed-mode failure requires calculation of mode mixity defined here as fraction of energy release that is mode I or $\phi = G_I/G$. Some early work on homogeneous beams suggested a method for partitioning G into G_I and G_{II} (Williams 1988), but that partitioning was at odds with numerical calculations for partitioning (Hutchinson and Suo 1992). Although a revised beam theory might eventually improve partitioning (Williams 2018), the only current method to partition with confidence is to use numerical methods. As mentioned above, FEA with quadratic elements converges very rapidly for energy release rate in beam fracture problems. But that convergence is only for *total* energy release rate. This author has observed that convergence for mode partitioning is much slower and may require very small elements. If the goal is a refined analysis based on numerical methods, those FEA calculations must use high resolution. If the goal is an analytical expression for design (*e.g.*, Eq. (17)), such analysis may not be able to account for mixed-mode loading. The total G approach, however, is still useful provided G_c is chosen appropriately.

The second issue is that even if $\phi(\xi)$ could be calculated (*i.e.*, mode mixity as a function of notch depth), one has to assume a failure criterion $f(G_I, G_{II}, G_{Ic}, G_{IIc})$. Many such criteria have been proposed, notably in the related problem of composite delamination (Reeder 1992). Unfortunately, there are insufficient mixed-mode CLT failure data to justify selection among these criteria. If that situation changes, mixed-mode loading effects could be included. For illustration, assume a simple linear criterion where failure occurs when

$$\frac{G_I}{G_{Ic}} + \frac{G_{II}}{G_{IIc}} = \left(\frac{\phi(\xi)}{G_{Ic}} + \frac{1-\phi(\xi)}{G_{IIc}} \right) G = 1$$

or failure occurs when total G reaches a critical value of

$$G = G_c = \frac{G_{Ic}}{\psi + \phi(\xi)(1-\psi)}$$

where $\psi = G_{Ic}/G_{IIc}$ is ratio of mode I to mode II toughness. Substituting this G_c into Eq. (17) would give a limit load calculation that accounts for mixed-mode loading. For example, the FEA calculations in Fig. 4 were partitioned into modes resulting in failure prediction when $G = (1.65 \pm 0.55)G_{Ic}$ for all notch depths assuming $\psi = 1/3$. In these calculations, $\phi(\xi)$ varied from 0.18 to 0.89 with extreme values at top of the first 0° layer and bottom of the last 0° layer; besides these locations $\phi(\xi)$ was between 0.42 and 0.72 predicting failure when $G = (1.43 \pm 0.20)G_{Ic}$. The FEA calculations were low resolution and therefore may have inaccurately partitioned G, but they likely provide an estimate of variations in G at failure due to mode-mixity effects. Using the lower end (*e.g.*, $G_c = 1.1G_{Ic}$) would give conservative limit load calculations.

The above calculations assumed all 0° layers and all 90° layers were identical and that the CLT plate was at some equilibrium temperature and moisture content such that ΔT and Δc were the same in all layers. The assumption of identical layers was needed to derive analytical results for mechanical properties such as Eqs. (7), (9), and (11). The assumption of constant ΔT and Δc was needed to derive analytical results for residual stress properties such as Eqs. (8), (9), and (11). But real CLT may have layers with differing properties (*e.g.*, using different grades of timber in different layers), may have temperature and moisture contents that vary with position in the plate, may have properties that depend on variable temperature and moisture content, and may have residual stress effects altered by mechanosorptive behavior of wood (Hunt 1994). Although accounting for these effects severely complicates analytical predictions, most can trivially be included

in a spreadsheet or in simple laminated beam software. In brief, the CLT plate is described by $2n-1$ arbitrary layers where layer j has properties E_j, α_j, β_j, ΔT_j, Δc_j, and t_j. These properties are substituted into the laminated beam analysis in the appendix to find $C_\kappa^{(i)}$, $\kappa_{res}^{(i)}$, and $\sigma_{res}^{(i)\,2}$. Finally, these beam results are used in general energy release rate equations to predict failure. To additionally handle temperature or moisture gradients within a single layer, each layer can be subdivided into enough layers such that ΔT_j and Δc_j in those sublayers provide a piecewise-linear approximation to the gradients.

The following example uses a general beam analysis approach to assess the role gradients in ΔT and Δc. Imagine a CLT plate at equilibrium $c_0 = 12\%$ moisture content whose surface is subjected to wet conditions (*e.g.*, standing water if exposed to rain during construction) or dry conditions (*e.g.*, seasonal reductions in humidity). Because diffusion through wood is slow, surface moisture content will change faster than core moisture contnet. An exact 1D solution for moisture content through the thickness can be derived as a Fourier series, but here a simple expression was used to qualitatively describe moisture gradients in a plate of thickness h with $y = 0$ at the center of the plate:

$$\Delta c(y) = (c_{surf} - c_0)\frac{\cosh\left(\frac{y}{\eta}\right)}{\cosh\left(\frac{h}{2\eta}\right)}$$

Here c_{surf} is surface concentration boundary condition and η is a parameter that characterizes extent of moisture transport through wood. In diffusion theory, η would be directly related to $D \times time$ where is D is transverse moisture diffusion constant for the wood. To compare moisture gradients to uniform moisture content at the same total moisture content, the average moisture content as function of η is:

$$\langle \Delta c(\eta) \rangle = \frac{1}{h}\int_{-h/2}^{h/2} \Delta c(y)\, dy = (c_{surf} - c_0)\frac{2\eta}{h}\tanh\frac{h}{2\eta}$$

Figure 9A shows sample gradients in Δc for $\eta = 20$, 50, and 100 for $c_{surf} = 24\%$ moisture content along with their average values.

Figure 9B shows calculations of P_{fail} for a five-layer CLT plate using properties in Table 2 with $t_0 = 40$ mm, $\lambda = 1$, and $G_c = 350$ J/m^2 for $\eta = 20$, 50, and 100. The solid lines give predictions by analytical modeling for constant $\langle \Delta c(\eta) \rangle$, which were 2.4%, 5.78%, and 9.14% for the three values of η. With the input $\beta_t - \beta_L = 0.26$, these conditions correspond to $\Delta\varepsilon_{res} = 0.62\%$, 1.50%, and 2.38%, respectively. The dashed lines show the change in failure due to gradients in moisture content. These calculations were done by dividing each layer into 19 sublayers with identical properties except changing the moisture expansion coefficient in the 90° layers to

$$\beta_j = \frac{\beta_t \Delta c(y_j)}{\langle \Delta c(\eta) \rangle}$$

where y_j is midpoint of sublayer j. With this change, composite beam analysis using $\beta_j \langle \Delta c(\eta) \rangle$ will equal $\beta_t \Delta c(y_j)$ and provide the appropriate level of moisture effect in layer j. The top half of Fig. 9B is for $c_{surf} = 24\%$ such that $\Delta\varepsilon_{res} > 0$ and the arms always separate while the bottom half is for $c_{surf} = 0$ such that some notches are in contact (and when needed, the P_{fail} calculations switched to using the contact energy release rate in Eq. (5)). For most notches, failure load in the presence of gradients is higher than for

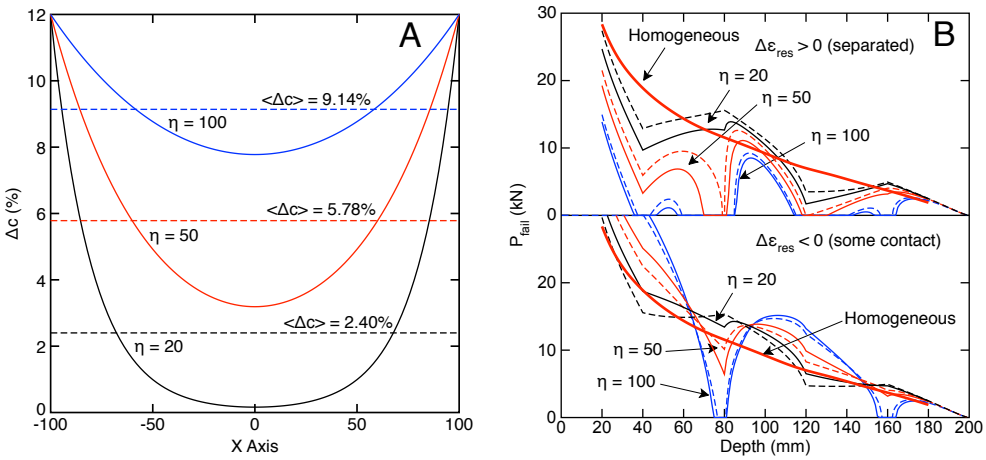

Figure 9. A. Illustrative moisture content gradients for three values of η. The horizontal lines show average moisture contents for each eta. B. Failure loads predicted by equating Eq. (4) or Eq. (5) to $G_c = 350$ J/m^2 for three values of η. The solid lines are for constant Δc; the dashed lines are for moisture content gradients. The thick line is for a homogeneous beam. The top is for $\Delta\varepsilon_{res} > 0$ and separated arms. The bottom is for $\Delta\varepsilon_{res} < 0$ that has contacting arms at some notch depths (see Eq. (3)).

a plate with the corresponding uniform moisture content. As expected, the result with gradients approaches the uniform result as η increases. Notice that failure load when $\Delta\varepsilon_{res} < 0$ is always higher then when $\Delta\varepsilon_{res} > 0$ and often higher than homogeneous plate predictions. Nevertheless, certain notch depths are still prone to delamination even when $\Delta\varepsilon_{res} < 0$ (*e.g.*, at 80 mm or at the second interface from the bottom). For design purposes, failure loads calculated with a constant Δc and $\Delta\varepsilon_{res} > 0$, which is the basis for Eq. (17), would provide conservative failure predictions.

Other position-dependent layer properties may affect failure. Perhaps most important would be position-dependent toughness. For design calculations, G_c should be set to the local toughness at the notch root and consider effects of temperature and moisture content on that toughness. If that root is at in an interface between two layers, G_c should be set to $\min(G_{c,wood}, G_{c,adhesive})$ or failure is determined by the weaker material near that notch root. Note that while a poor adhesive (or a region near the notch with incomplete adhesive coverage) could result in premature failure, even a perfect adhesive with infinite toughness would not prevent failure by a crack path that diverts into a wood layer near the interface.

This analysis treated the 90° layers as homogeneous layers with properties given by transverse properties of wood. A common CLT manufacturing method glues the faces between layers, but not the edges between timber within a layer. These non-glued edges may affect failure at a notch, especially if a non-bonded edge is near the notch root. One crude approach to modeling non-glued edge effects would be to replace properties of 90° layers with effective properties that account for those edges. Some equations for evaluating E_t, G_{RS}, α_t, and β_t for 90° layers as function of distance between non-glued edges in those layers is given in Nairn (2017). Note that this calculation should anticipate the formation of additional cracks that tend to form over time in installed CLT (Nairn 2018).

Finally, properties and failure within the 90° layers depend on the end-grain patterns of the timber in those layers. For flat-sawn or radially-sawn timber, the layer properties for beam analysis would be tangential (T) or radial (R) properties of the wood, respectively. For most wood species, $E_R > E_T$, $\alpha_R < \alpha_T$. and $\beta_R < \beta_T$. These relations suggest radially-

sawn timber would be preferred, but that conclusion would depend on fracture toughness for crack growth in the x direction. Wood fracture literature designates these crack paths as TR fracture for radially-sawn timber and RT fracture for flat-sawn timber (Johnson 1973). Because it is difficult to control crack-propagation direction in the transverse plane, few results are available for comparing TR to RT propagation toughness (Shir Mohammadi and Nairn 2014). Furthermore, in practice, timber end-grain will be neither flat sawn nor radially sawn, but instead will have curved end grains including some end grains near or through a tree's pith. A recommended approach to assessing the role of timber end-grain effects is to measure effective CLT toughness values using tests on notched CLT plates with various end-grain patterns.

4. Conclusions

Equations (4) and (5) together with specific results for notch roots within 0° layers (Eqs. (9) and (10)) or within 90° layers (Eqs. (11) and (12)) provide accurate, analytical expressions for predicting delamination failure of notched CLT plates. Equation (17) uses swelling conditions and separated arms to provide a conservative design guide for CLT plates. The important additions in these equations were to account for both heterogeneity and residual stresses. The presented calculations show that expected levels of residual stresses caused by variations in environmental conditions play a significant role in notch failure. Some options to reduce residual stress effects (if notches are needed) are to use thinner layers, to avoid notch roots near layer interfaces, and to prefer notch roots near the middle of 0° layers. An unacceptable option is to rely on design guides that ignore residual stresses. That approach would be equivalent to building a timber structure in Sweden and thinking it is acceptable to ignore snow loads.

Acknowledgements

This work was made possible by the endowment for the Richardson Chair in Wood Science and Forest Products. I thank Erik Serrano for pointing out the issue of notched CLT beams and sending information on recent experimental results, and both Erik Serrano and Lech Muszyński for helpful comments.

References

Conrad, M.P., Smith, G.D., and Fernlund, G., 2003. Fracture of solid wood: A review of structure and properties at different length scales. *Wood and Fiber Science*, 35 (4), 570–584.

Forest Products Laboratory, 2010. *Wood Handbook: Wood as an engineering material*. General technical report FPL-GTR-190. Madison, WI: U.S. Dept. of Agriculture, Forest Service, Forest Products Laboratory.

Friberg, A., 2017. Bärförmåga för KL-trä med urtag – provning och beräkningsmetoder (in Swedish) (Load-bearing capacity of CLT with notches – testing and calculation methods). Bachelor's Thesis, LTH School of Engineering, Lund University, Helsingborg, Sweden.

Gustafsson, P., 1988. A study of strength of notched beams. *In*: *Proc. of the CIB-W18 Meeting 21*, 01. Parksville, Canada, Paper No. CIB-W18/21-10-1.

Hashemi, S., Kinloch, A.J., and Williams, J.G., 1990. The analysis of interlaminar fracture in uniaxial fibre reinforced polymer composites. *Proc. R. Soc. Lond.*, A427, 173–199.

Hashin, Z., 1969. Theory of composite materials. *In*: H.L. F. W. Wendt and N. Perrone, eds. *Mechanics of composite materials*. Pergamon Press, 201–242.
Hunt, D.G., 1994. Present knowledge of mechanosorptive creep of wood. in Creep in timber structures. Report of RILEM Technical Committee 112-TSC, Pages 73-97. London, UK.
Hutchinson, J.W. and Suo, Z., 1992. Mixed mode cracking in layered materials. *Advances in Applied Mechanics*, 29, 63–191.
Johnson, J.A., 1973. Crack initiation in wood plates. *Wood Science*, 6 (2), 151–158.
Nairn, J.A., 1997. Fracture mechanics of composites with residual thermal stresses. *J. Appl. Mech.*, 64, 804–810.
Nairn, J.A., 2006. On the calculation of energy release rates for cracked laminates with residual stresses. *Int. J Fract. Mech.*, 139 (267–293).
Nairn, J.A., 2011. Generalized crack closure analysis for elements with arbitrarily-placed side nodes and consistent nodal forces. *Int. J. Fracture*, 171, 11–22.
Nairn, J.A., 2017. Cross-laminated timber properties including effects of non-glued edges and additional cracks. *European Journal of Wood and Wood Products*, 75 (6), 973–983.
Nairn, J.A., 2018. Predicting layer cracks in cross-laminated timber with evaluations of strategies for suppressing them. *European Journal of Wood and Wood Products*, in revisions.
Nairn, J.A., 2019. Material point method (NairnMPM) and finite element analysis (NairnFEA) open-source software. http://osupdocs.forestry.oregonstate.edu/index.php/Main_Page [Accessed 24 July 2019].
Reeder, J.R., 1992. An evaluations of mixed mode failure criteria. NASA Techincal Memorandum 104210, February.
Schapery, R.A. and Davidson, B.D., 1990. Prediction of energy release rate for mixed-mode delamination using classical plate theory. *Appl. Mech. Rev.*, 43, S281–S287.
Schniewind, A.P. and Pozniak, R.A., 1971. On the fracture toughness of Douglas Fir wood. *Engineering Fracture Mechanics*, 2, 223–233.
Serrano, E., 2018. Cross laminated timber plates with notches – analyses based on fracture mechanics. *In*: G. Dill-Langer, ed. *Timber: Bonds, Connections, Structures. Commemorative Publication Honoring Simon Aicher on the Occasion of his 65th Birthday*. Material Testing Institute, University of Stuttgart, Germany, 111–126.
Serrano, E., Gustafsson, P.J., and Danielsson, H., 2019. Prediction of load-bearing capacity of notched cross laminated timber plates. *In*: 6^{th} *Meeting of International Network on Timber Engineering Research (INTER)*. Tacoma, Wash, USA, 26-29 August.
Shir Mohammadi, M. and Nairn, J.A., 2014. Crack propagation and fracture toughness of solid balsa used for cores of sandwich composites. *Journal of Sandwich Structures and Materials*, 16 (1), 22–41.
Stanzl-Tschegg, S.E., Tan, D.M., and Tschegg, E.K., 1996. Mode II fracture tests on spruce wood. *Mokuzai Gakkaishi/Journal of the Japan Wood Research Society*, 42 (7), 642–649.
Williams, J.G., 1988. On the calculation of energy release rates for cracked laminates. *Int. J. Fract.*, 36, 101–119.
Williams, J.G., 2018. Personal communication.
Wilson, E., Shir Mohammadi, M., and Nairn, J.A., 2013. Crack propagation fracture toughness of several wood species. *Advances in Civil Engineering Materials*, 2 (1), 316–327.
Wolfram Research, 2017. *Mathematica 11.1*. Champaign, IL.
Yoshihara, H., 2004. Mode II R-curve of wood measured by 4-ENF test. *Engineering Fracture Mechanics*, 71 (13-14), 2065–2077.

Appendix

The effective properties of the three sublaminates in Fig. 1 can be determined from laminated beam analysis that is included here for completeness. For a laminated beam under axial strain ε_0 and curvature κ, the axial strain as a function of y is $\varepsilon(y) = \varepsilon_0 - \kappa y$, where

$\kappa > 0$ corresponds to curvature upward, $y = 0$ is the mid-plane of the sublaminate. The axial stress in each layer, including residual stresses, is

$$\sigma_{xx}(y) = E(y)\big(\varepsilon_0 - \kappa y - \alpha(y)\Delta T - \beta(y)\Delta c\big)$$

where $E(y)$, $\alpha(y)$, and $\beta(y)$ are the position-dependent modulus, thermal expansion coefficient, and moisture expansion coefficient in the x direction. Integrating these stresses, total axial force, N, and bending moment, M, can be written as

$$\begin{aligned} N = \int_A \sigma_{xx}(y)\, dA &= -S^{(i)}_{n1}\kappa + S^{(i)}_{n2}\varepsilon_0 - S^{(i)}_{n3} \\ M = -\int_A \sigma_{xx}(y) y\, dA &= S^{(i)}_{m1}\kappa - S^{(i)}_{m2}\varepsilon_0 + S^{(i)}_{m3} \end{aligned}$$

where for a layered structure, the integrals simplify to

$$S^{(i)}_{n1} = S^{(i)}_{m2} = B\sum_{j=1}^{n_i} E_j t_j \bar{y}_j \qquad S^{(i)}_{n2} = B\sum_{j=1}^{n_i} E_j t_j \qquad S^{(i)}_{m1} = B\sum_{j=1}^{n_i} E_j t_j \left(\bar{y_j}^2 + \frac{t_j^2}{12}\right)$$

$$S^{(i)}_{n3} = B\sum_{j=1}^{n_i} E_j(\alpha(y)\Delta T + \beta(y)\Delta c)t_j \quad S^{(i)}_{m3} = B\sum_{j=1}^{n_i} E_j(\alpha(y)\Delta T + \beta(y)\Delta c)t_j \bar{y}_j$$

Here E_j, α_j, β_j, t_j, and $\bar{y}_j$ are the x-direction modulus, x-direction thermal expansion coefficient, x-direction moisture expansion coefficient, thickness, and midpoint of layer j in sublaminate i with n_i total layers. Inverting these equations leads to Eq. 1 where

$$C^{(i)}_{\kappa} = \frac{S^{(i)}_{n2}}{S^{(i)}_{m1}S^{(i)}_{n2} - S^{(i)}_{n1}S^{(i)}_{m2}} \quad C^{(i)}_{\varepsilon} = \frac{S^{(i)}_{m1}}{S^{(i)}_{m1}S^{(i)}_{n2} - S^{(i)}_{n1}S^{(i)}_{m2}} \quad D^{(i)} = \frac{S^{(i)}_{m2}}{S^{(i)}_{m1}S^{(i)}_{n2} - S^{(i)}_{n1}S^{(i)}_{m2}}$$

$$\kappa^{(i)}_{res} = \frac{S^{(i)}_{m2}S^{(i)}_{n3} - S^{(i)}_{n2}S^{(i)}_{m3}}{S^{(i)}_{m1}S^{(i)}_{n2} - S^{(i)}_{n1}S^{(i)}_{m2}} \qquad \varepsilon^{(i)}_{res} = \frac{S^{(i)}_{m1}S^{(i)}_{n3} - S^{(i)}_{n1}S^{(i)}_{m3}}{S^{(i)}_{m1}S^{(i)}_{n2} - S^{(i)}_{n1}S^{(i)}_{m2}}$$

These results are general laminated beam analysis and can be used with any mixture of layer properties. The analytical results quoted in the text of this paper are special cases of these equations for alternating 0° and 90° layers common in CLT plates.